Natural Resources Research (© 2026)
https://doi.org/10.1007/s11053-026-10694-z

Original Paper

Seismic Porosity Estimation Using Geologically-Informed Seismic Attributes and a Kriging-Enhanced Random Forest: Application to a Shallow-Marine Carbonate Reservoir

Mohammadali Rezaei,[1,2,4] **Andrew D. La Croix**,[1] **Mohammad Emami Niri**,[3] **and Omid Asghari**[2]

Received 28 September 2025; accepted 20 April 2026

Reliable property modeling is vital for Earth resource development, and seismic data can provide secondary variables to improve accuracy. However, seismic-integrated models remain uncertain due to inherent limitations in seismic data such as the cumulative effects of signal processing and attribute computation. In this study, we aimed to estimate a high-accuracy 3D secondary variable for porosity modeling from seismic attributes using a kriging-enhanced random forest (RF). This approach leverages the ensemble learning capabilities of RF to effectively handle limited training data, while incorporating the ability of kriging to account for spatial correlation. Prior to implementing this model, we developed an innovative workflow to correct seismic attributes based on geological trends. This workflow generated geologically informed seismic attributes by vertically correcting seismic attributes in areas of lower quality, while preserving their original lateral trends. We applied our methodology to a late Albian–early Turonian shallow-marine carbonate reservoir with a complex diagenetic history. After creating geologically informed seismic attributes, we used them, along with porosity well logs, as inputs for the kriging-enhanced RF model. This model calculated the mean of decision trees through kriging estimation rather than the usual averaging method. To evaluate effectiveness, we compared it with a deep neural network, a kriging-enhanced deep neural network, and a standard RF. The kriging-enhanced RF produced porosity closer to blind-well values than other methods and captured complex heterogeneities, such as channels and differing reservoir qualities across sequences, making the porosity cube a reliable 3D trend for further geostatistical simulations.

KEY WORDS: Reservoir characterization, Stratigraphy, Gaussian process, Ensemble learning, Radial basis function, Spatial correlation.

[1]Sedimentary Environments and Analogues Research Group, Earth and Environmental Sciences, School of Science, University of Waikato, Hamilton 3240, New Zealand.
[2]Simulation and Data Processing Laboratory, School of Mining Engineering, University of Tehran, Tehran, Iran.
[3]Institute of Petroleum Engineering, School of Chemical Engineering, College of Engineering, University of Tehran, Tehran, Iran.
[4]To whom correspondence should be addressed; e-mail: mr1161@students.waikato.ac.nz

INTRODUCTION

A major challenge in characterizing the geological and geophysical properties of the Earth is that data collection is often expensive, time-consuming, and limited to a small number of sparse, unevenly distributed observations (Bai & Tahmasebi, 2021; Zhang et al., 2024; Tran et al., 2025).

Published online: 08 May 2026

However, Earth materials and structures are known to be spatially correlated (Journel and Huijbregts, 1978), allowing geostatistical methods to estimate values at unsampled locations by leveraging this spatial structure (Maxwell et al., 2021; Liu et al., 2022; Nwaila & Carranza, 2025; Nwaila et al., 2025). Incorporating secondary data can further improve geostatistical estimations, while minimizing uncertainty and addressing issues such as non-stationarity (Emery & Robles, 2009; Rezaei et al., 2024; Esteve et al., 2025).

3D seismic reflection data provide valuable subsurface imagery with broad spatial coverage, allowing detailed mapping of geological features, especially in regions between wells (Emami Niri & Lumley, 2016; Wang et al., 2020, 2024; Kamaruzaman et al., 2023, 2024; Leisi et al., 2024). Despite their utility, seismic data are limited by vertical resolution, usually on the order of tens of meters (Olutoki et al., 2024; Mishra et al., 2025). Integrating seismic data with petrophysical well logs enables better characterization of subsurface variability, with demonstrated applications in coalbed methane development (Liu et al., 2024), petroleum geology (Rezaei et al., 2023), petroleum engineering (Garcia et al., 2024), geothermal reservoir modeling (Feng et al., 2020), and CO_2 storage (Alalimi et al., 2022).

Seismic attributes play a key role in predicting and mapping reservoir characteristics, including facies distribution, lithology, pore-fluid content, and the spatial distribution of reservoir units. Seismic attributes enhance interpretive precision and provide deeper insights into subsurface geology (Emami Niri & Lumley, 2017; Wang et al., 2024; Ehsan et al., 2025; Lu et al., 2025). To incorporate the large-scale information embedded in seismic attributes into reservoir characterization, supervised machine learning (ML) techniques can be used to derive composite seismic attribute that serve as secondary variables for geostatistical modeling (Pyrcz & Deutsch, 2014). However, limited seismic sampling along well trajectories constrains most of ML, especially deep learning, that require large datasets (Olutoki et al., 2024; Zhang et al., 2025). By contrast, ensemble learning techniques such as XGBoost (eXtreme Gradient Boosting) and RF (random forest) offer a more robust option with small datasets (Zou et al., 2021; Mou et al., 2023; Maxwell et al., 2024). For recent examples of the application of ensemble learning methods in estimating porosity from seismic attributes, refer to Zou et al. (2021), Song et al. (2023), Ntibahanana et al. (2024), and Mohammad Hossain et al. (2024).

A common limitation of ML methods, including ensemble learning models, is the neglect of spatial correlation (Lv et al., 2021; Mohammadpour et al., 2023). As a result, hybrid approaches that integrate kriging with ML predictions have gained significant traction, demonstrating superior estimation accuracy compared to standalone ML models (Erten et al., 2022, 2025; Chen et al., 2023). Examples include combining ordinary kriging with neural network (Sergeev et al., 2019), ML mapping and regression kriging (Li et al., 2019), kriging-enhanced neural networks (Liu et al., 2020), hybrid geostatistical-ML models (Erten et al., 2023; Mohammadpour et al., 2024), and deep Gaussian process for spatial modeling (Gonçalves and Wellmann, 2025). Therefore, a combination of ensemble learning and kriging can be an effective approach for estimating porosity from seismic attributes and well logs. This strategy leverages the strengths of ensemble ML to address data limitations while also accounting for spatial correlation through kriging.

However, well-engineered attributes enable models to perform better and improve specific learning tasks. By utilizing domain knowledge alongside mathematical and statistical transformations, we can derive new features from raw data or enhance existing ones (Misra et al., 2020). Because seismic attributes are plagued with uncertainties due to errors in the velocity model, extensive signal processing, and attribute computation, it is crucial to apply corrections such as standardization and resampling to the seismic attributes (Khayer et al., 2022; Lin et al., 2024; Naseer, 2025; Verma et al., 2025).

In this study, we developed a workflow that corrects seismic attributes based on vertical porosity trends linked to sea-level fluctuations. These geologically informed attributes, combined with porosity well logs, were used to train an enhanced ensemble learning model. Our model integrated kriging within the RF aggregation process using a radial basis function (RBF) kernel to refine tree-wise predictions. This spatially aware ensemble approach outperformed standard models and deep learning baselines in blind well tests, producing a geologically consistent seismic porosity cube suitable for geostatistical simulation.

STUDY AREA AND GEOLOGICAL BACKGROUND

The study area is situated along the western portion of the Abadan Plain (Iran), a structural zone at the western end of the Zagros Fold-Thrust Belt (ZFTB) (McQuarrie, 2004). It encompasses several oil fields across an area of 22.4 km by 37.8 km. Within the Abadan Plain, the late Albian–early Turonian Sarvak Formation is the most significant carbonate reservoir interval (Asaadi et al., 2016). During late Cretaceous, the Sarvak Formation and its stratigraphic equivalents across the Arabian Plate were deposited on a vast shallow-marine carbonate platform, which included several intrashelf sub-basins (Fig. 1) (Vincent et al., 2015). This depositional interval was characterized by high sea levels on the Arabian Plate (Haq, 2014). However, this was interrupted by multiple phases of sea-level fall due to the combined effects of tectonics and eustatic changes. A sequence stratigraphic framework and associated relative sea-level curve for the Cretaceous successions of southwestern Iran has been developed by Van Buchem et al. (2006; see Fig. 2a).

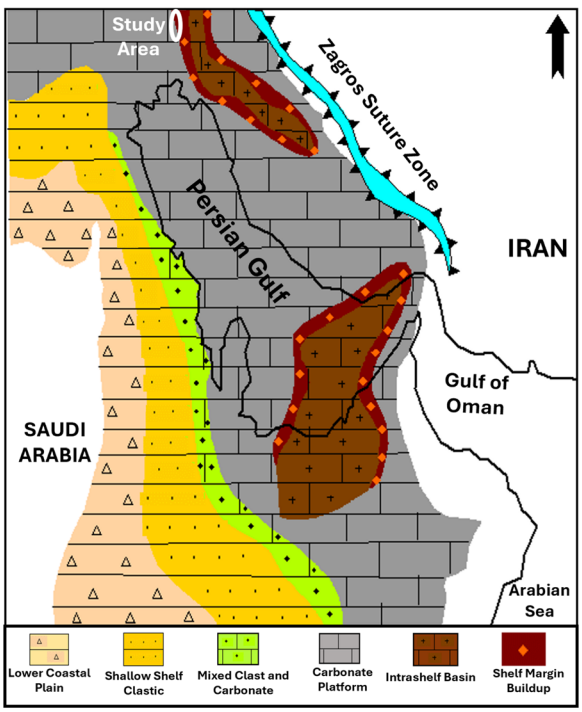

Figure 1. Paleogeographic map of Arabian Peninsula and adjacent areas during Cenomanian–Turonian (Upper Cretaceous) (modified from Du et al., 2015).

By interpreting sequence boundaries (SB) and maximum flooding surfaces (MF), Asaadi et al. (2016) identified four third-order sequences in the Sarvak Formation of the Abadan Plain (Fig. 2b). The first sequence (late Albian–lower Cenomanian), which comprises the lower Sarvak Formation, is 205 m thick. Its highstand system tract (HST) is 180 m thick and lies below the early Cenomanian disconformity and includes a ~ 120 m thick zone of grain-dominated facies affected by dissolution, exhibiting high porosity and permeability. The second sequence (mid-Cenomanian) is ~ 245 m thick and is bounded by the early and mid-Cenomanian disconformities. The interval has high reservoir quality, derived from both depositional facies and dissolution along the mid-Cenomanian disconformity. The third sequence (late Cenomanian), which constitutes the upper Sarvak Formation, is ~ 215 m thick. The HST of this sequence, which is ~ 170 m thick, contains two ~ 80 m rudist debris zones that are correlatable between wells, and serve as the main reservoir intervals. Finally, the fourth sequence (Turonian), which is ~ 25 m thick, consists mainly of mudstone and wackestone deposited in low-energy settings, but are not considered reservoirs. It is worth mentioning that this study focused on the second, third, and fourth sequences of the Sarvak Formation, which represent the primary oil intervals.

Rapid sea-level change during the Cenomanian–Turonian led to complex diagenesis in the region (Asaadi et al., 2016), including karstification, dissolution, cementation, recrystallization, and dedolomitization. Channel deposits formed during platform exposure or flooding events, later filled with muddy carbonates or clays associated with poor reservoir quality. Channel lithology and size vary with depth and location (Rezaei et al., 2023), adding to reservoir heterogeneity (Grélaud et al., 2010).

MATERIALS AND METHODS

Dataset

This study focused on the upper part of the Sarvak Formation because it is a key reservoir interval with clearly defined channel deposits. Our modeling used data from 26 wells, with 7 wells (21% of the total) serving as blind wells for model validation. The dataset consisted of standard wireline log suites (i.e., gamma ray, neutron, density, resis-

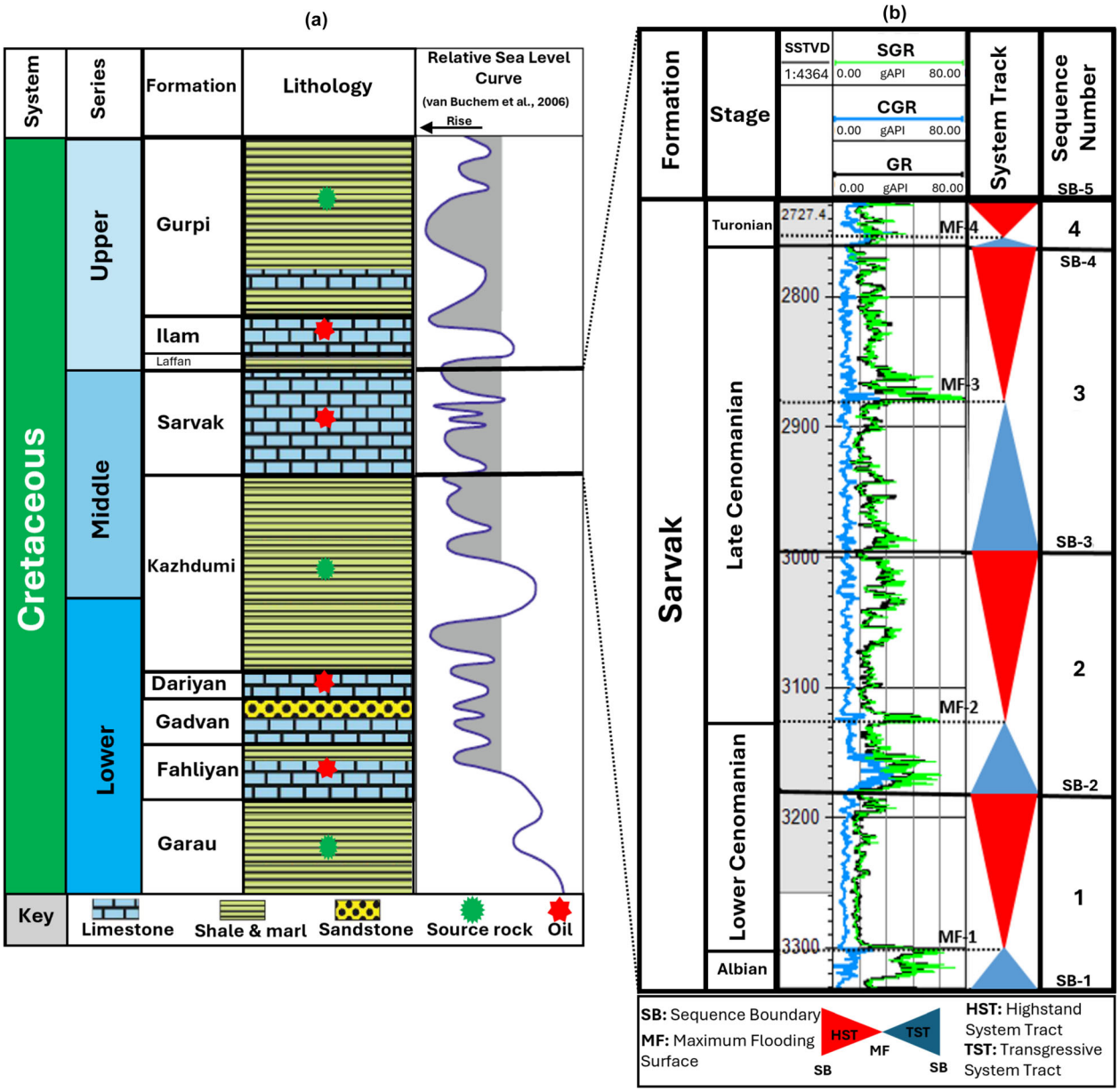

Figure 2. (**a**) Cretaceous lithostratigraphy and relative sea-level curve of central Zagros region (modified from Esrafili-Dizaji et al., 2015 and Van Buchem et al., 2006). (**b**) Four distinct third-order sequences in Sarvak Formation and representative gamma ray well log from studied field (modified from Asaadi et al. 2016).

tivity, sonic), including interpreted effective porosity logs. Additional geophysical data included depth maps of the interpreted horizons and a depth-converted seismic cube. Figure 3a displays a structural cross section of the relative acoustic impedance attribute, overlain by effective porosity logs, whereas Figure 3b displays the 3D seismic data.

Geological Correction of Seismic Attributes

Several volumetric attributes were extracted from the 3D seismic data. Relative acoustic impedance, gradient, instantaneous phase, and first time-derivative were determined to correlate most closely with porosity and were able to identify complex geological features, such as channels (Supplementary Fig. S1). To quantify these rela-

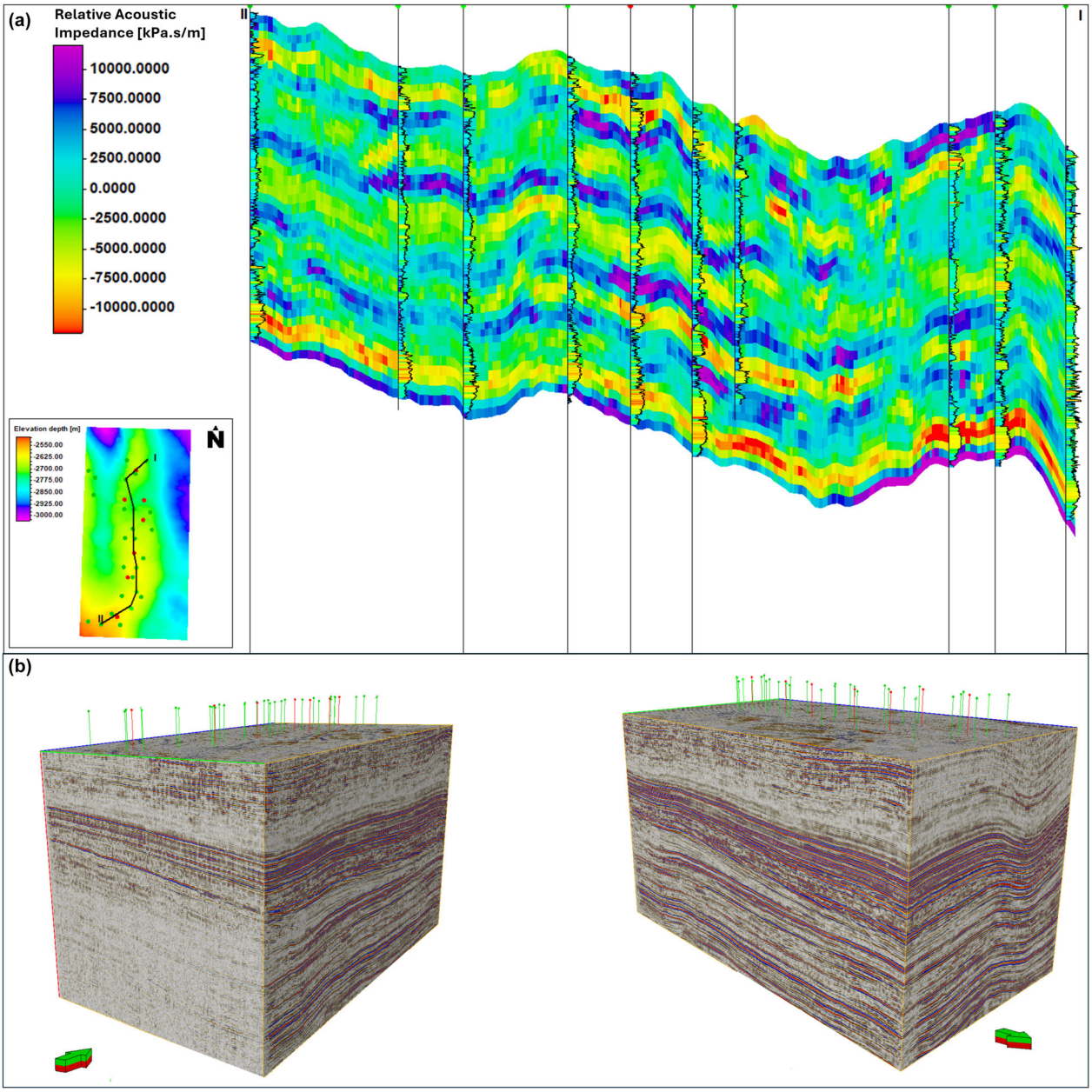

Figure 3. (**a**) Structural cross section of relative acoustic impedance in the Sarvak Formation, overlain with effective porosity logs from ten wells. Inset map of Sarvak Formation shows location of wells used for modeling (in green) and blind wells (in red), overlain on a depth structure map. (**b**) 3D view of seismic data in two different directions.

tionships, correlation coefficients were calculated between effective porosity logs and seismic attributes at each well location. The resulting values were interpolated into correlation coefficient maps using an interpolation method (Kelishami et al., 2022). In some areas, seismic attributes showed poor correlation with porosity, primarily due to geological heterogeneity and velocity model errors (Fig. 4). To address this challenge, we enhanced the seismic attribute correlation by identifying well locations with a high attribute-porosity correlation and then propagating these values using universal kriging, incorporating a vertical trend calculated from the general variation of effective porosity well logs in the Z direction. Figure 5 shows effective porosity and shale volume well logs along with the overall vertical

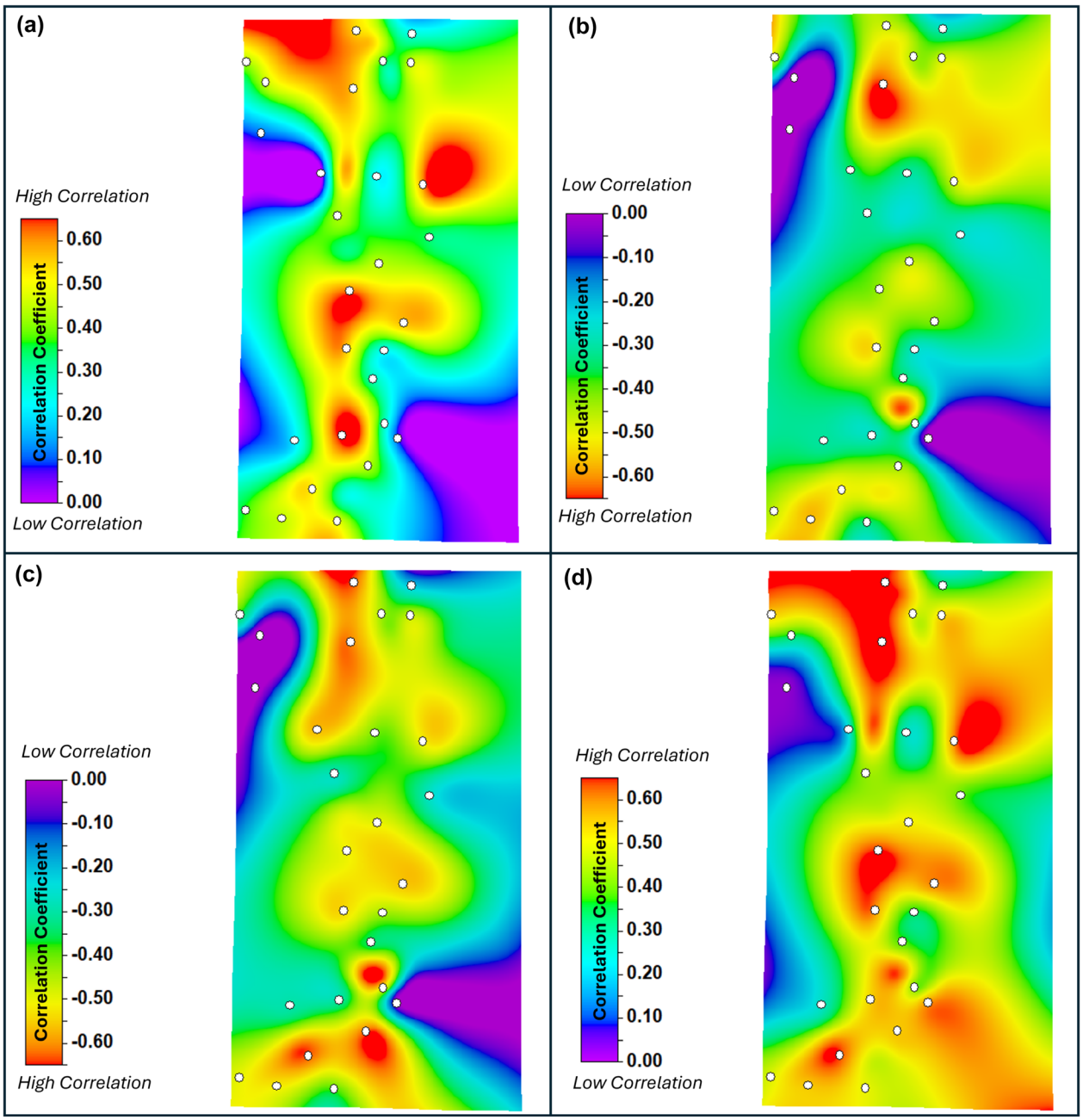

Figure 4. Maps of correlation coefficient between effective porosity and (**a**) gradient (positive correlation), (**b**) relative acoustic impedance (negative correlation), (**c**) instantaneous phase (negative correlation), and (**d**) first time-derivative seismic attributes (positive correlation).

porosity trend. These variations in porosity closely align with four third-order sequences discussed above in section *Study Area and Geological Background*, reflecting sea-level changes. During universal kriging, errors between the vertical trend and seismic attributes at well locations were calculated and distributed through collocated cokriging, with the seismic attribute used as a trend. This step improved the vertical quality of the attributes while maintaining their original spatial trends. The main steps of this process are illustrated in Figure 6.

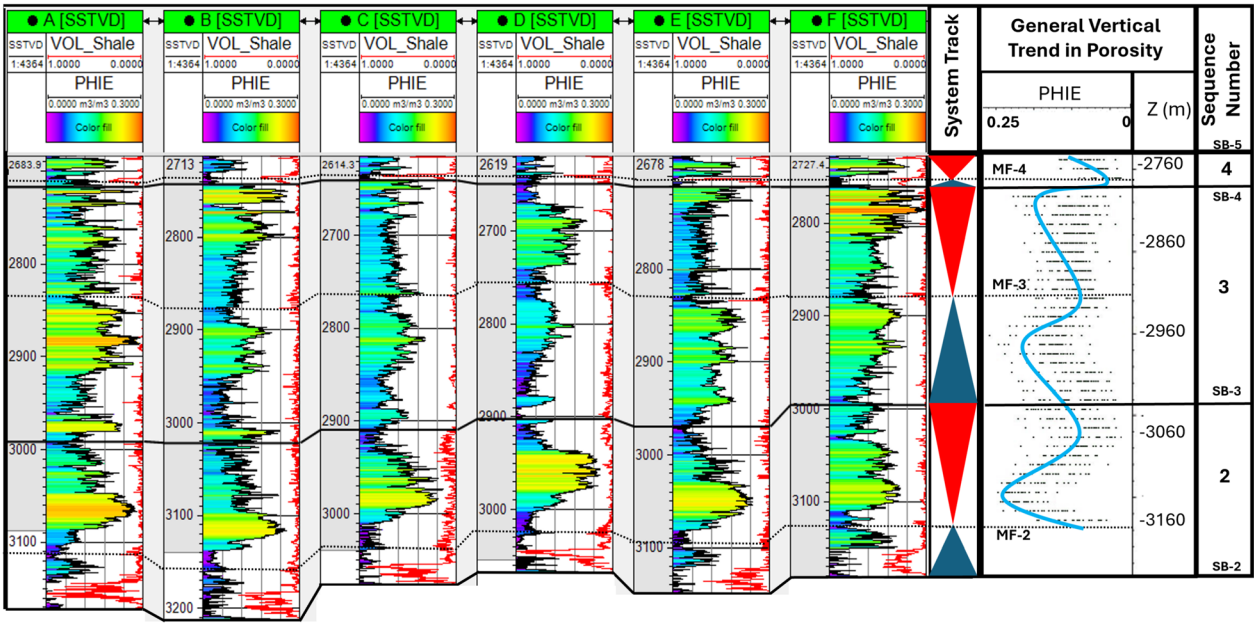

Figure 5. Vertical effective porosity variation in second, third, and fourth sequences of Sarvak Formation in study area.

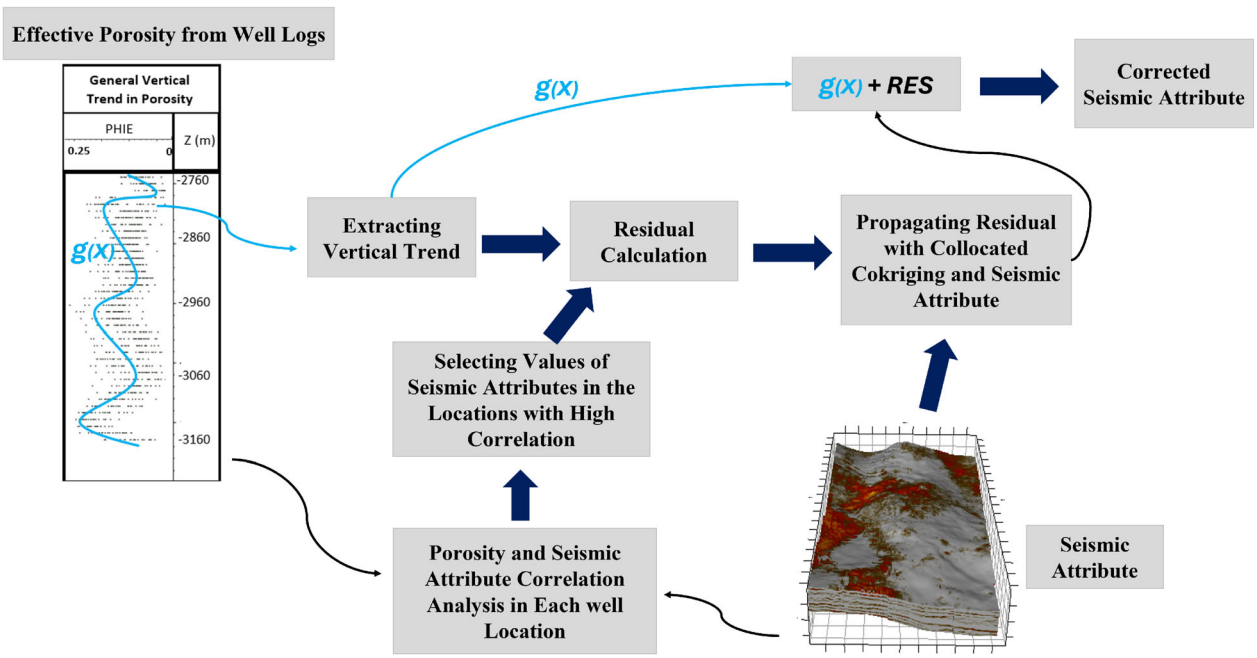

Figure 6. Main steps in geological correction of a seismic attribute using proposed workflow.

Seismic Porosity Estimation Using Kriging-Enhanced Random Forest

Corrected seismic attributes were used in a kriging-enhanced RF model to generate a seismic porosity cube. Figure 7 illustrates a 3×3 grid, where two of the cells contain well-log porosity data. It explains how kriging-enhanced RF (with five trees) was used to estimate seismic porosity throughout the entire grid. An expanded explanation of the theoretical underpinnings of this framework is presented in the Appendix. To train the model, we used the effective porosity logs along with corrected seismic attribute values at well locations, with 25% of the training dataset used for validation. The RF implementation used the Scikit-learn library in Python (Pedregosa et al., 2012). Model performance was assessed using R^2 and mean squared error (MSE) on both the training and validation datasets to identify the optimal number of decision trees, k. Results from 100 experiments indicated that more than 80 trees provided no significant improvement in performance (Supplementary Fig. S2). Therefore, the final model used 80 decision trees.

Next, predicted values from the 80 decision trees were extracted for each training sample and used as input to the kriging process. Several kernels were tested (e.g., exponential, Matern, rational quadratic, RBF), and the RBF was chosen as it resulted in the lowest MSE and highest R^2 values (Supplementary Fig. S3).

Optimal hyperparameters were determined by minimizing the negative logarithm of the marginal likelihood (-Q), optimized using both Adam (Kingma and Ba, 2014) and stochastic gradient descent (SGD) (Bottou, 2010). Both reached a similar minimum, but Adam converged faster (Supplementary Fig. S4), and so it was adopted. Model generalization was further assessed with 10-fold cross-validation (Fig. 8), which showed that predictions aligned closely with observations and that overfitting was not occurring.

Finally, the trained model was applied across the simulation grid to establish the seismic attribute-porosity relationship throughout the study area. This yielded a 3D porosity cube for the Sarvak Formation.

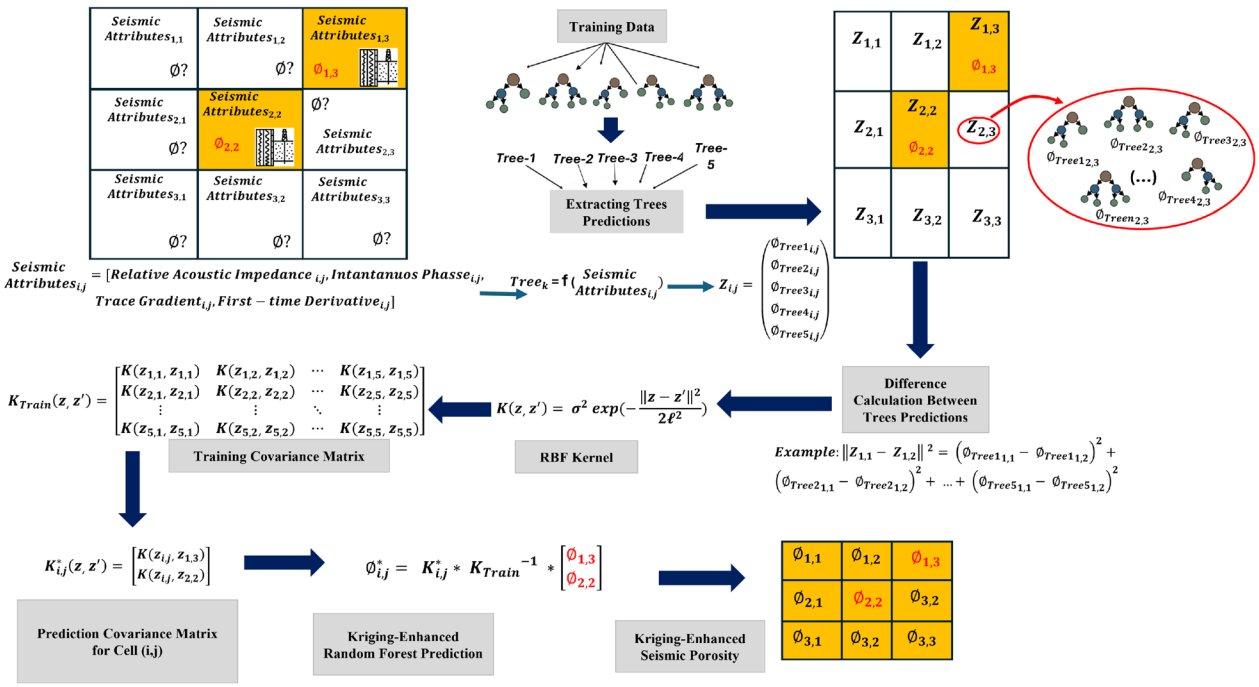

Figure 7. Main steps in kriging-enhanced random forest for seismic porosity estimation.

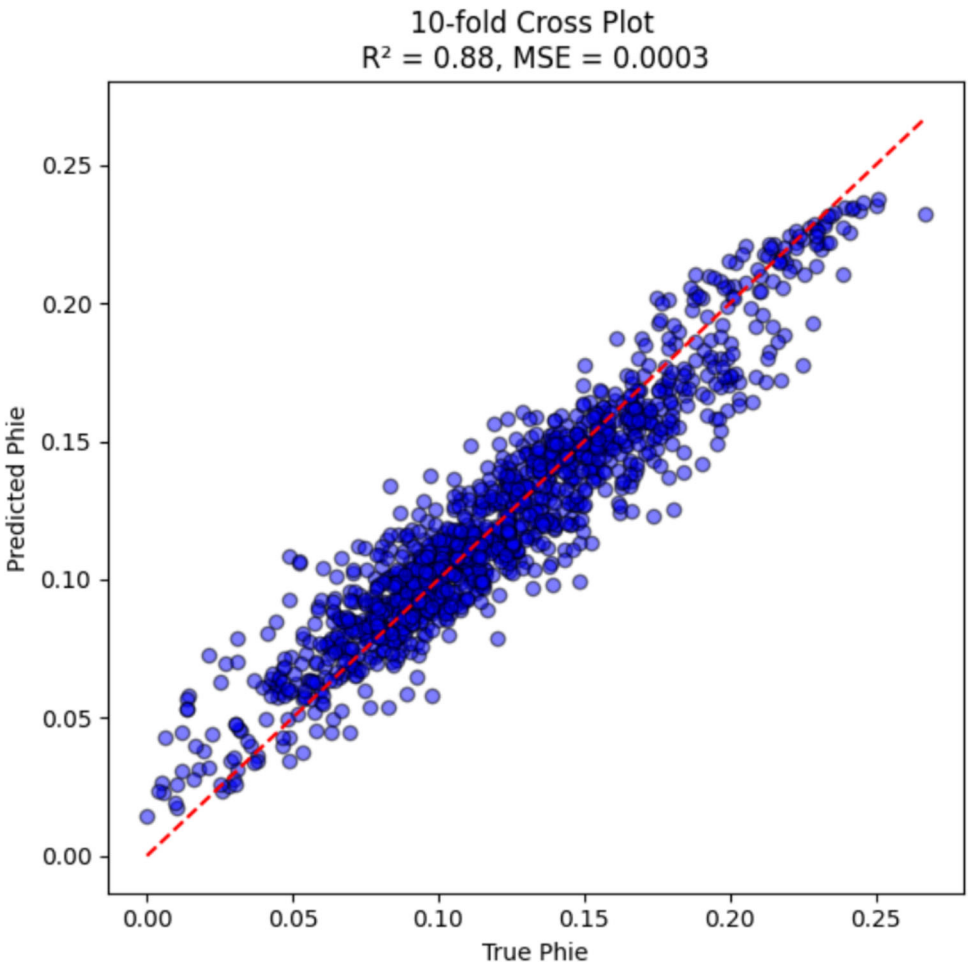

Figure 8. Comparison of actual versus simulated porosity values using kriging-enhanced random forest method. Results were derived from 10-fold cross-validation.

RESULTS AND DISCUSSION

Porosity represents the capacity of a potential reservoir to store subsurface fluids such as oil and natural gas. Consequently, precise porosity estimation is critical for effective exploration and production, as it directly influences reservoir characterization, recovery efficiency, and field development strategies. This paper proposes an innovative workflow for 3D seismic porosity prediction in heterogeneous carbonate reservoirs by developing geologically informed seismic attributes and using them in a kriging-enhanced RF model. As a result, the seismic correction process improved the correlation coefficient between effective porosity and the seismic attributes notably. Specifically, Figure 9 illustrates two seismic attributes at a well location, where their initial values showed a poor correlation with porosity. The correction process improved the correlation coefficient for trace gradient from 0.21 to 0.53, and for instantaneous phase from − 0.19 to − 0.57. Additionally, the horizontal cross section of seismic attributes before and after the correction showed that, while correlation with effective porosity increased, the horizontal trends remained consistent, allowing complex features such as channels to be clearly identified (Fig. 10, Supplementary Fig. S5). Histograms of the initial and corrected seismic attributes also overlapped closely, confirming that the correction preserved their distribution (Fig. 11). Together, these results demonstrated that the workflow improves seismic attribute quality without changing their original spatial trends. In other words, when seismic attributes are

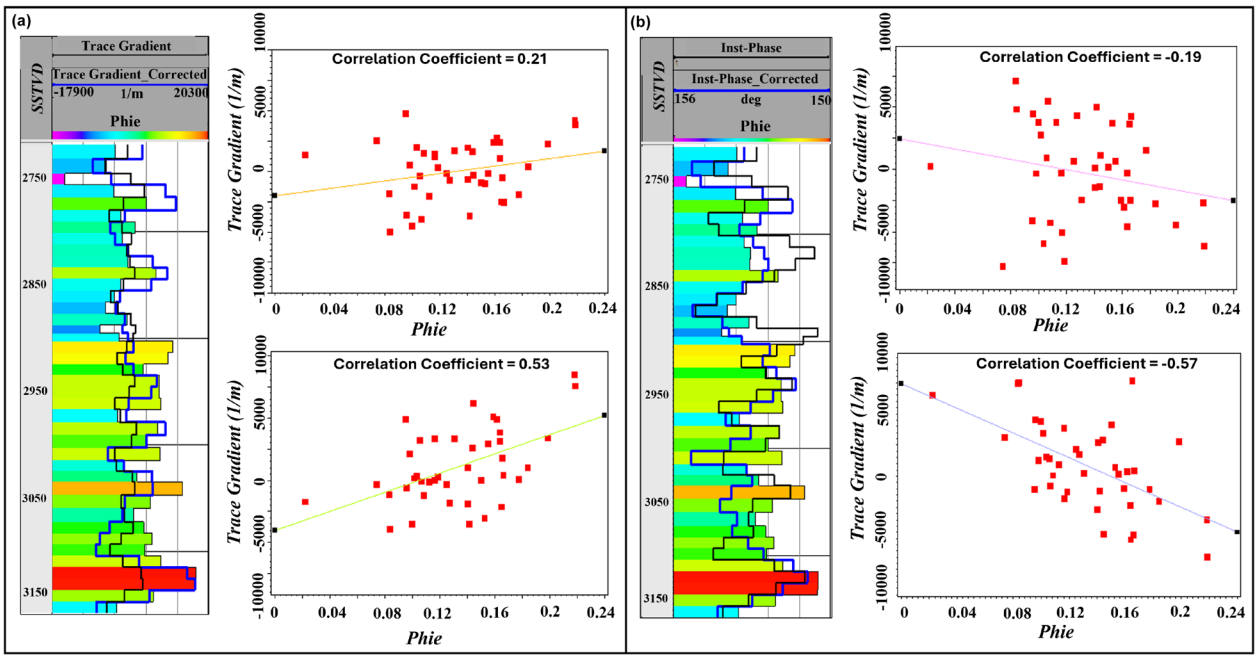

Figure 9. (**a**) Trace gradient and (**b**) instantaneous phase attributes before (black line; top graph) and after (blue line; bottom graph) correction in a well location.

guided by geological trends, such as the vertical variation in effective porosity, they become significantly more useful, especially in where data quality is low.

These findings underscore the importance of aligning seismic attributes with geological controls to improve their utility in reservoir characterization. The efficacy of using seismic attributes for reservoir characterization is inherently sensitive to factors such as data quality, velocity model accuracy, and basin-specific geological complexity. In some cases, these limitations may render attributes unreliable or even ineffective (Liner et al., 2004; Marfurt & Alves, 2015; González et al., 2025). Reservoir properties, however, are strongly influenced by fluctuations in sea level (Chen et al., 2024; Naseer, 2024; Curtis et al., 2025). By deriving geological constraints from effective porosity well logs and applying the proposed seismic attribute correction based on geological constraints, this study demonstrated a viable approach to overcoming interpretive challenges and enhancing the reliability of seismic attributes in future studies.

After generating the geologically informed seismic attributes, we used them as inputs in a kriging-enhanced RF model to create a seismic porosity cube (Fig. 12a) for the selected intervals of the Sarvak Formation. The cross sections in Figure 12b, compare the actual porosity values at blind well locations with the estimated porosity cube derived from the kriging-enhanced RF. The estimated porosity values at blind wells align closely with the actual porosity values, confirming model reliability. To evaluate the effectiveness of our technique, we compared our results with four alternative scenarios (Fig. 13). In the first scenario, initial seismic attributes were used in a deep neural network. In the second scenario, the same neural network was trained with corrected attributes, and its correlation with actual effective porosity was improved by 23%. The third model was a kriging-enhanced deep neural network, in which kriging replaced the linear transfer function in the output layer. This addition incorporated spatial continuity in the data and better handled non-linear behavior, raising correlation to 57% (Fig. 13). A standard RF model served as the fourth scenario, which resulted in a prediction accuracy of 68%. The kriging-enhanced RF outperformed all alternatives, with the correlation between estimated and actual porosity reaching 83%.

The performance across three different blind wells is shown in Figure 14. In each case, the pre-

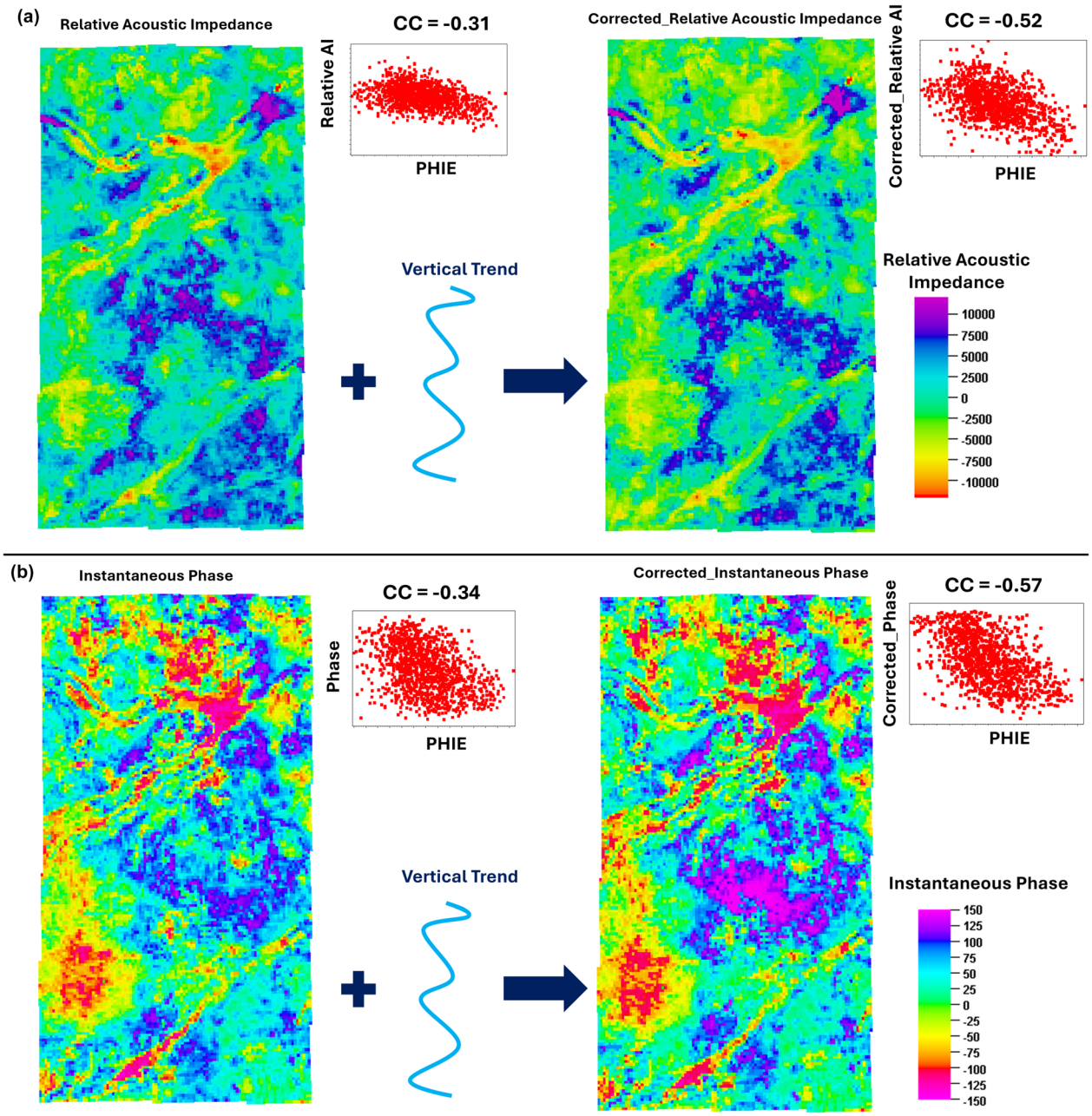

Figure 10. Structural depth sections of (**a**) relative acoustic impedance and (**b**) instantaneous phase seismic attributes before and after correction. Cross plots illustrate correlation between seismic attributes and porosity well logs prior to and following the correction.

dicted effective porosity (red line) closely follows the true values (blue line). Uncertainty estimates, represented by the standard deviation (red dashed) and 95% confidence intervals (yellow shading), captured variability and consistently bracketed the true values. These comparative results highlight the importance of hybrid ensemble learning–geostatistical approaches in seismic reservoir characterization, particularly when well-log data is limited. While supervised algorithms have advanced seismic interpretation by integrating multiple attributes (Yue et al., 2019; Li et al., 2020), their reliance on dense training datasets remains a challenge. Ensemble methods like RF offer improved gener-

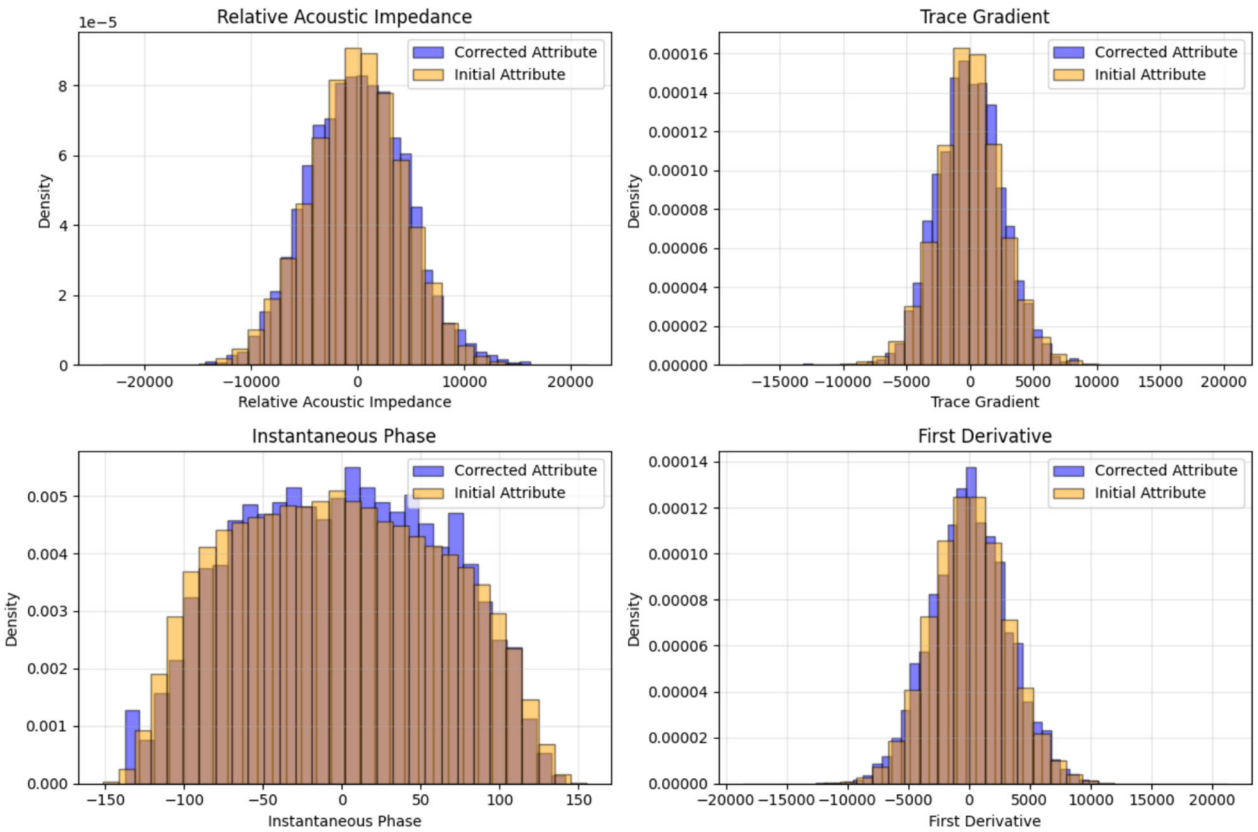

Figure 11. Histograms of seismic attributes before (orange) and after (blue) geological correction. Light brown color represents overlapping values.

alization with fewer samples, yet they overlook spatial continuity. By embedding kriging into the RF framework, our proposed workflow effectively bridged this gap, capturing both attribute-driven variability and spatial structure. The resulting seismic porosity cube not only demonstrated superior predictive accuracy compared to deep neural networks and standard ensemble models, but also provided well-constrained uncertainty estimates across blind wells. These findings validated the utility of kriging-enhanced ensemble learning for generating reliable 3D porosity trends, which can serve as robust secondary data in geostatistical simulations and support more informed reservoir development strategies.

The estimated seismic porosity showed strong correlation with measured porosity values while effectively capturing complex geological features (see cross sections in Fig. 15). A vertical cross section through the second sequence of the Sarvak Formation illustrates porosity variations, including carbonate channels with diverse shapes and qualities. Channelized zones in sequence 2 are typically filled with higher porosity sediments compared to the surrounding background, though in some cases porosity is lower. The observed porosity variations within sequence 2, aligned well with prior studies by Asaadi et al. (2016), in which reservoir quality in sequence 2 is largely attributed to primary depositional characteristics and dissolution processes.

A further vertical cross section compares porosity in the third and fourth sequences of the Sarvak Formation with estimated seismic porosity across two wells (Fig. 16). The porosity cube

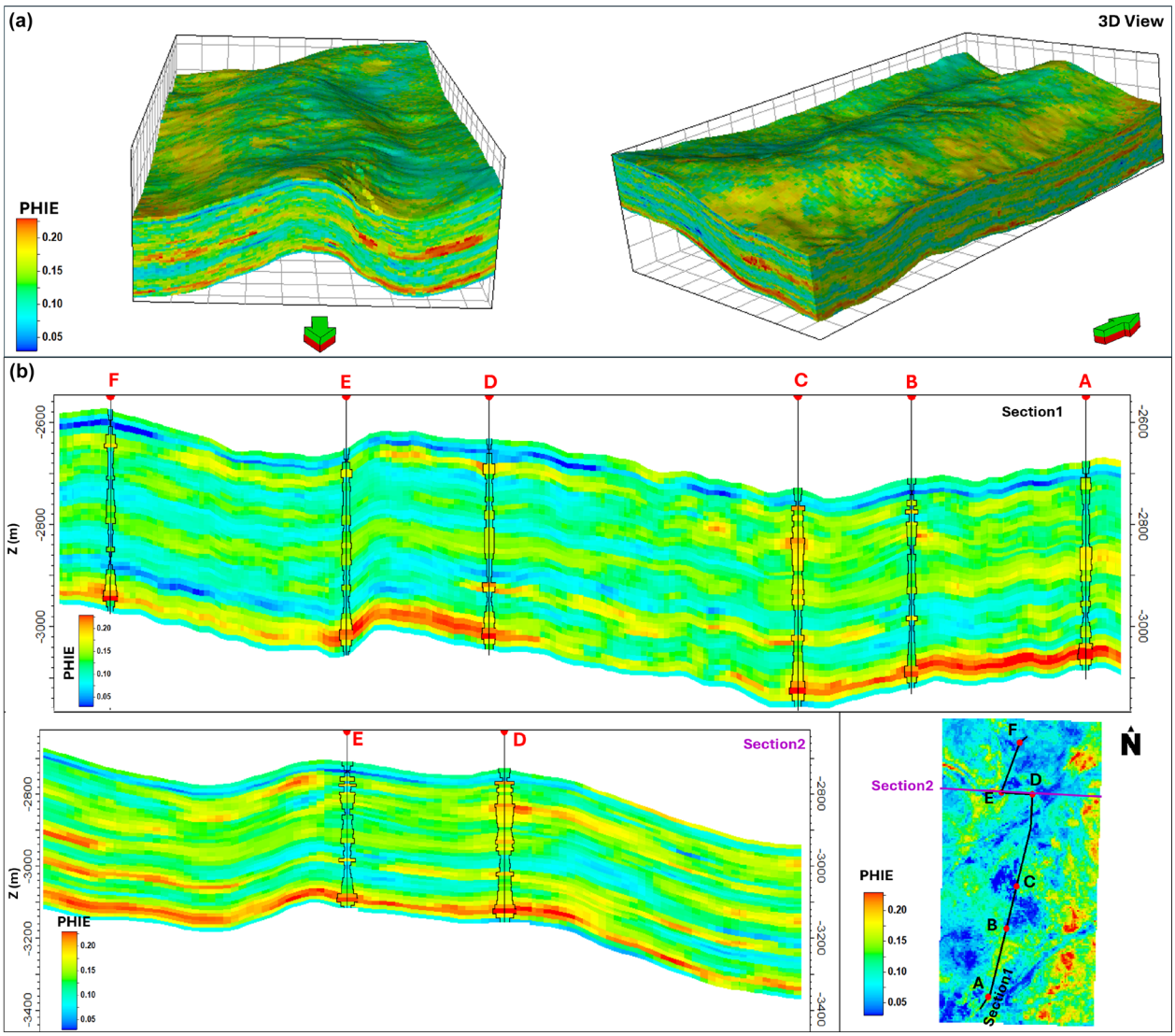

Figure 12. (**a**) 3D view of estimated seismic porosity cube in two different directions. (**b**) Comparison between estimated seismic porosity cube and real porosity values in blind wells.

demonstrated a high degree of consistency with well data, while also resolving complex geological features such as large incisions. These results confirmed the effectiveness of our approach to characterizing a heterogeneous carbonate reservoir and reflect seismic porosity cube's sensitivity to diagenetic alterations such as dissolution and calcite cementation. This was consistent with the classification by Sabouhi et al. (2022), where zones with enhanced dissolution and development of intergranular and vuggy pores—characteristic of DG-3 and DG-4 diagenetic classes—show higher porosity values, whereas areas affected by calcite cementation (DG-0 and DG-1) tend to display lower reservoir quality. Moreover, the variable porosity in channels of different sequences and intervals was well aligned with

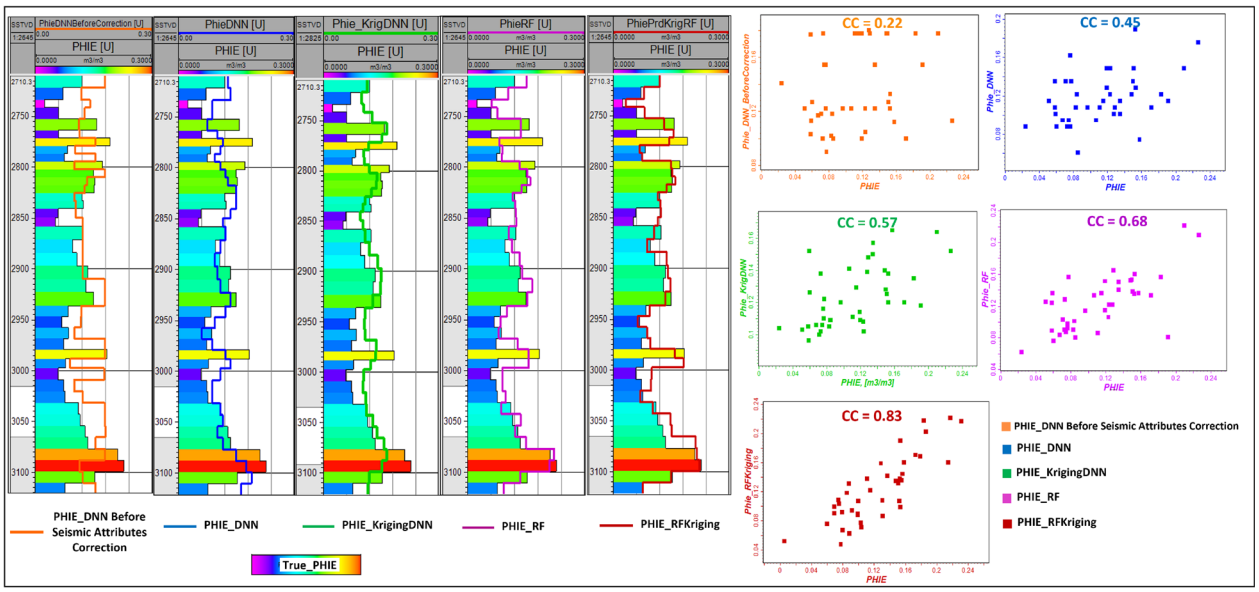

Figure 13. Comparison between measured effective porosity in a blind well and model estimates from: a deep neural network using initial seismic attributes (orange), a deep neural network using corrected seismic attributes (blue), a kriging-enhanced deep neural network (green), a standard random forest (pink), and kriging-enhanced random forest (red).

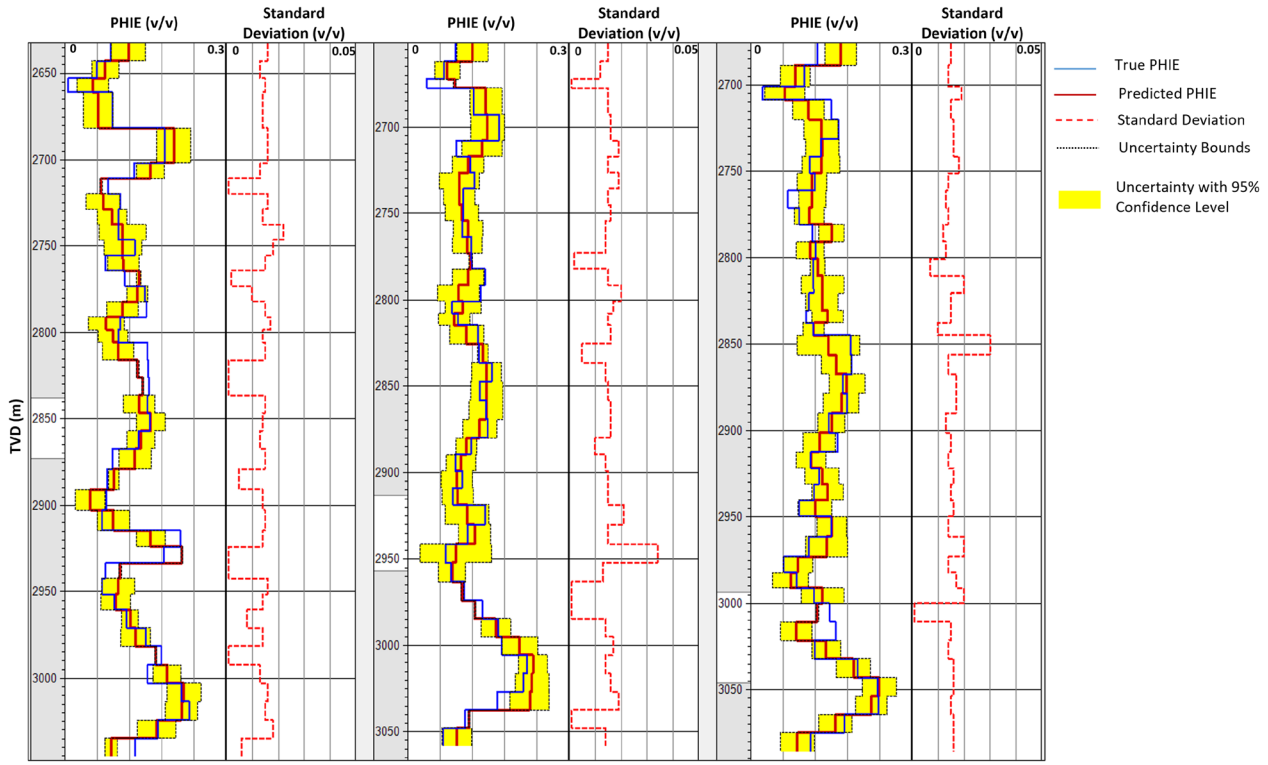

Figure 14. Predicted versus actual effective porosity across three blind wells. For each well, left track displays true and predicted values along with 95% confidence intervals, while right track shows predicted standard deviation.

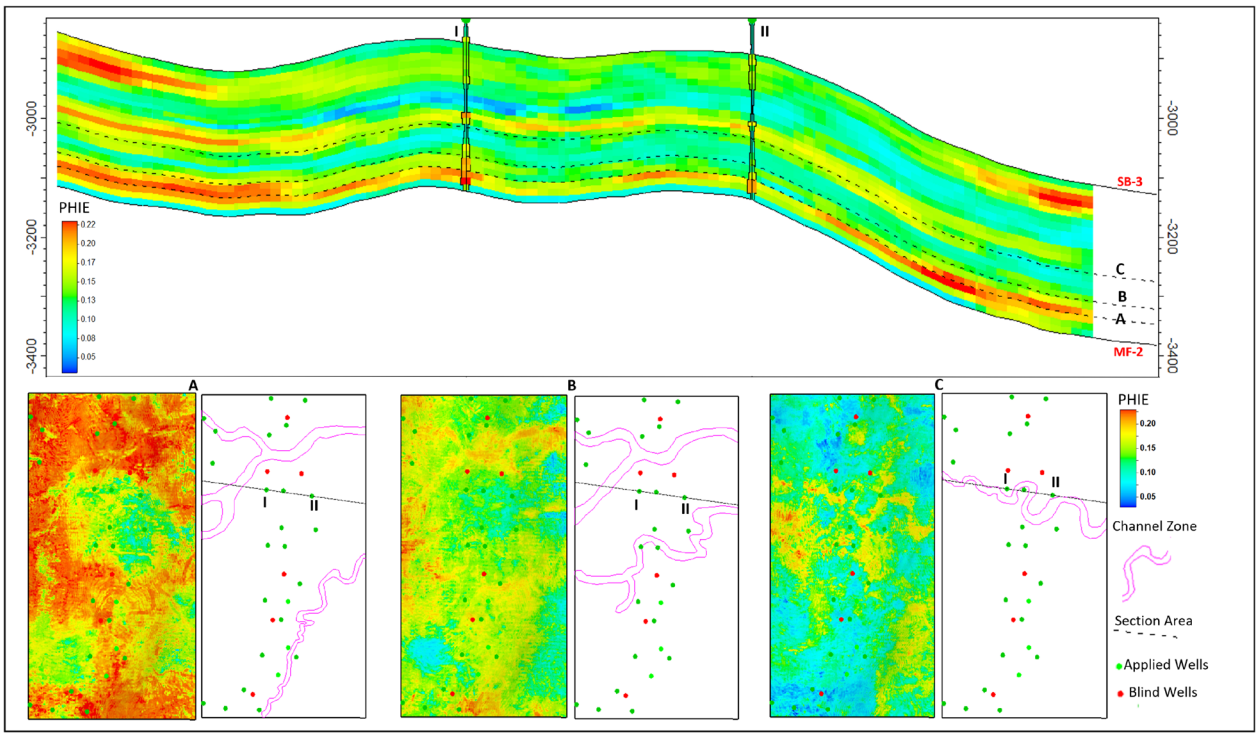

Figure 15. Cross sections from estimated porosity cube from second sequence of Sarvak Formation.

the facies model developed by Rezaei et al. (2023). Overall, the seismic porosity cube not only provided a realistic basis for decision-making tasks but can also serve as an efficient 3D trend for geostatistical simulations, especially in predicting reservoir quality across poorly sampled regions.

CONCLUSIONS

In this study, the results from blind wells indicated that the geological adjustment of seismic attributes improved estimation accuracy by up to 30%. The RF ensemble approach outperformed a deep neural network, yielding higher prediction accuracy in blind wells. Ultimately, the application of the kriging-enhanced RF produced a seismic porosity cube that exhibited over 80% correlation with actual porosity values in blind wells. Using this model, we combined the ensemble learner's ability to handle data scarcity with kriging's capacity to account for spatial continuity. Our approach effectively highlighted significant quality variations within the reservoir, such as channel geobodies exhibiting porosity values lower or higher than the surrounding reservoir background across different stratigraphic sequences, as well as considerable porosity variations in non-channelized sections. Overall, the pro-

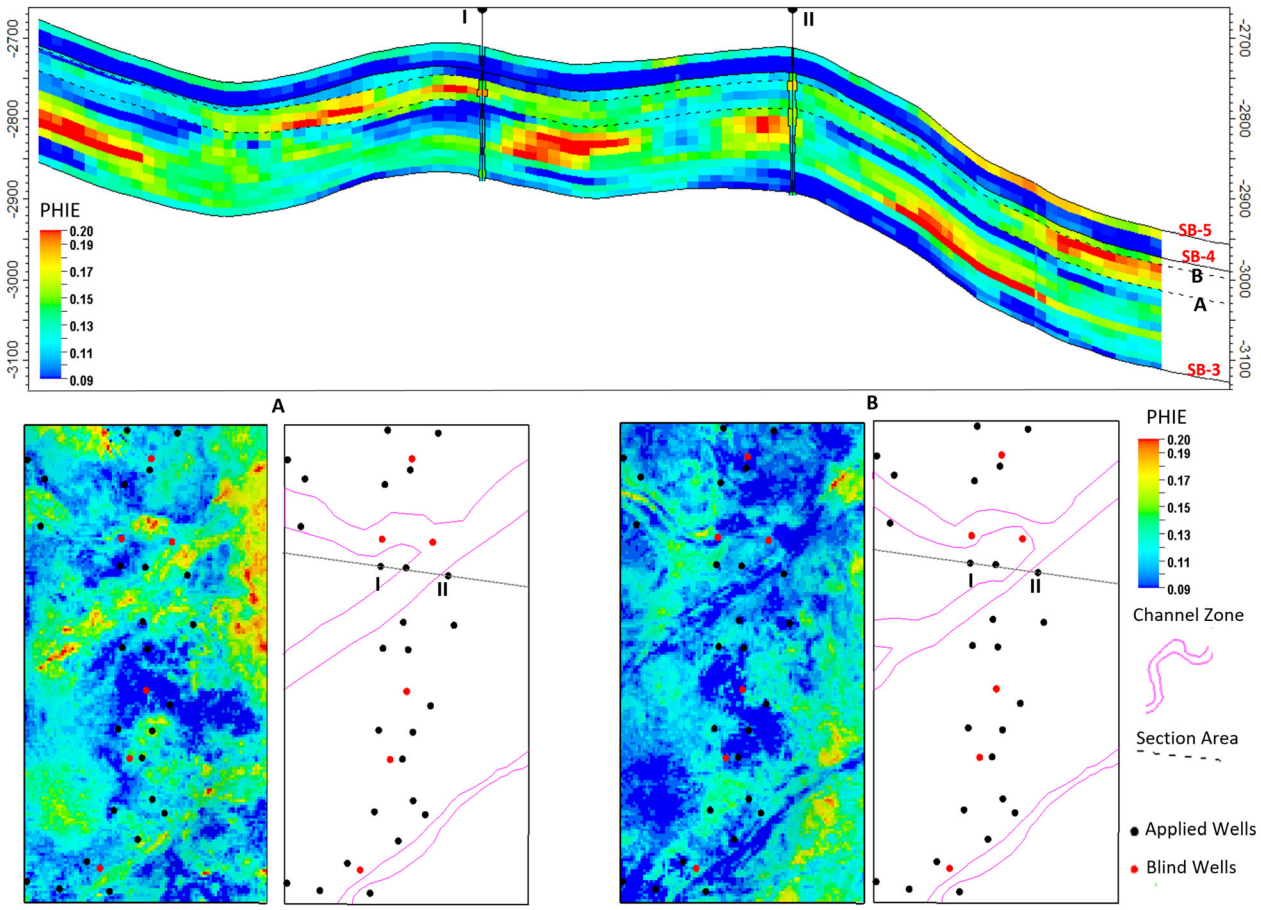

Figure 16. Cross sections from estimated porosity cube in third and fourth sequences of Sarvak Formation.

posed workflow offers a practical methodology for improving reservoir characterization in geophysically challenging environments.

FUNDING

Open Access funding enabled and organized by CAUL and its Member Institutions.

DECLARATIONS

Conflict of Interest The authors declare that they have no known competing financial interests or personal relationships that could have appeared to influence the work reported in this paper.

OPEN ACCESS

APPENDIX

In this study, we employed the RF algorithm as an ensemble learning method to create a 3D seismic porosity cube. To achieve this, we trained the corrected seismic attributes at well locations using porosity well logs as target variables. After establishing a reliable relationship at these well locations, we applied this relationship to the entire 3D grid. Additionally, to account for spatial correlation, we replaced the averaging process in the RF with a kriging process. To do this, after training the RF on the training data, we extracted predictions from each individual tree for both the training and testing datasets. This creates the matrices of X_{train} and X_{test} with dimensions $N \times K$ (where N is the number of training samples and K is the number of tress), and represents the predictions made by one tree. The output corresponding to these inputs is y_{train} with dimensions of $N \times 1$. In the next step, the kriging model was trained on the input data X_{train} and their corresponding outputs y_{train}. The posterior of the prediction is highly dependent on the kriging hyperparameters θ. These hyperparameters are typically optimized by maximizing the log marginal likelihood (LML), given by:

$$\begin{aligned}\mathcal{L}(\theta) &= \log p(y|X,\theta) \\ &= -\frac{1}{2}y^T\left(K+\sigma_n^2 I\right)^{-1}y - \frac{1}{2}\log|K \\ &\quad + \sigma_n^2 I\Big|\frac{n}{2}\log(2\pi)\end{aligned} \tag{1}$$

where σ_n^2 and I denote the noise variance and identity matrix, respectively. Moreover, K is the covariance matrix of the Gaussian process (x), which for n training points is defined as:

$$K(x,x') = \begin{bmatrix} K(x_1,x_1) & K(x_1,x_2) & \cdots & K(x_1,x_n) \\ K(x_2,x_1) & K(x_2,x_2) & \cdots & K(x_2,x_n) \\ \vdots & \vdots & \ddots & \vdots \\ K(x_n,x_1) & K(x_n,x_2) & \cdots & K(x_n,x_n) \end{bmatrix} \tag{2}$$

The covariance matrix is formed using a kernel applied to the training inputs X. In this study, we used the RBF kernel, also known as the Gaussian kernel, which is a commonly used covariance function in Gaussian processes. It is defined as:

$$K(x,x') = \sigma^2 \exp\left(\frac{\left\|x - x'^2\right\|}{2l^2}\right) \tag{3}$$

where ℓ is the length scale, and σ^2 represents the overall variance of the training inputs X.

After maximizing the marginal likelihood of the observed outputs given the inputs, we made predictions of y_* using the model. The predictive distribution (mean and variance) at new points is given by:

$$y_*|X_{train}, y_{train}, X_{test} \sim \mathcal{N}\left(\mu_*, \sigma_*^2\right) \tag{4}$$

where

$$\mu_* = K(X_{test}, X_{train})K\left(X_{traing}\right)^{-1}y \tag{5}$$

$$\begin{aligned}\sigma_*^2 &= K(X_{test}, X_{test}) \\ &\quad - K(X_{test}, X_{train})K(X_{train})^{-1}K(X_{test}, X_{train})\end{aligned} \tag{6}$$

We calculated the R^2 for both the training and testing datasets to evaluate the model's performance. After obtaining satisfactory R^2 values, we applied the kriging-enhanced RF model (which was trained at wells' locations) to the complete set of 3D seismic attributes, which allowed us to generate a seismic porosity cube.

SUPPLEMENTARY INFORMATION

The online version contains supplementary material available at https://doi.org/10.1007/s11053-026-10694-z.

REFERENCES

Alalimi, A., AlRassas, A. M., Vo Thanh, H., Al-qaness, M. A., Pan, L., Ashraf, U., Al-Alimi, D., & Moharam, S. (2022). Developing the efficiency-modeling framework to explore the potential of CO2 storage capacity of S3 reservoir, Tahe oilfield, China. *Geomechanics and Geophysics for Geo-Energy and Geo-Resources, 8*, 128.

Assadi, A., Honarmand, J., Moallemi, S. A., & Abdollahie-Fard, I. (2016). Depositional environments and sequence stratigraphy of the Sarvak Formation in an oil field in the Abadan Plain, SW Iran. *Facies, 62*, 1–22.

Bai, T., & Tahmasebi, P. (2021). Accelerating geostatistical modeling using geostatistics-informed machine learning. *Computers & Geosciences, 146*, 104663.

Bottou, L. (2010). Large-scale machine learning with stochastic gradient descent. In: Lechevallier, Y., Saporta, G. (eds) *Proceedings of COMPSTAT'2010*. Physica-Verlag HD.

Chen, L., Xiong, M., Tan, X., Chen, X., Zheng, J., Yang, Y., Jing, C., & Wang, G. (2024). Coupling mechanism between sea level changes and pore heterogeneity of marine shale reservoirs driven by astronomical orbital cycles: Lower Silurian Longmaxi shale in the Upper Yangtze area, South China. *Marine and Petroleum Geology, 160*, 106590.

Chen, W., Ding, J., Wang, T., Connolly, D. P., & Wan, X. (2023). Soil property recovery from incomplete in-situ geotechnical test data using a hybrid deep generative framework. *Engineering Geology, 326*, 107332.

Curtis, A., Bloem, H., Wood, R., Bowyer, F., Shields, G. A., Zhou, Y., Yilales, M., & Tetzlaff, D. (2025). Natural sampling and aliasing of marine geochemical signals. *Scientific Reports, 15*, 760.

Du, Y., Zhang, J., Zheng, S., Xin, J., Chen, J., & Li, Y. (2015). The rudist buildup depositional model, reservoir architecture and development strategy of the Cretaceous Sarvak formation of Southwest Iran. *Petroleum, 1*, 16–26.

Ehsan, M., Chen, R., Abdelrahman, K., Manzoor, U., Hussain, M., Ullah, J., & Zaheer, A. M. (2025). Application of petrophysical analysis, rock physics, seismic attributes, seismic inversion, multi-attribute analysis, and probabilistic neural networks for estimating petrophysical parameters for source and reservoir rock evaluations in the Lower Indus Basin, Pakistan. *Natural Resources Research*. https://doi.org/10.1007/s11053-025-10550-6.

Emami Niri, M., & Lumley, D. E. (2016). Probabilistic reservoir property modeling jointly constrained by 3D-seismic data and hydraulic-unit analysis. *SPE Reservoir Evaluation & Engineering, 19*(02), 253–264.

Emami Niri, M., & Lumley, D. E. (2017). Initialising reservoir models for history matching using pre-production 3D seismic data: Constraining methods and uncertainties. *Exploration Geophysics, 48*, 37–48.

Emery, X., & Robles, L. N. (2009). The seismic signature and geothermal potential of the Schwechat Depression in the Vienna Basin, Austria, from ambient noise tomography. *Geothermics, 127*, 103211.

Erten, G. E., Erten, O., Karacan, C. Ö., Boisvert, J. B., & Deutsch, C. V. (2023). Merging machine learning and geostatistical approaches for spatial modeling of geoenergy resources. *International Journal of Coal Geology, 276*, 104328.

Erten, G. E., Mokdad, K., da Silva, C. Z., Nisenson, J., Brandao, G., & Boisvert, J. (2025). Ensemble machine learning geostatistical hybrid models for grade control. *Mathematical Geosciences, 57*, 499–522.

Erten, G. E., Yavuz, M., & Deutsch, C. V. (2022). Combination of machine learning and Kriging for spatial estimation of geological attributes. *Natural Resources Research, 31*, 191–213.

Esrafili-Dizaji, B., Rahimpour-Bonab, H., Mehrabi, H., Afshin, S., Kiani Harchegani, F., & Shahverdi, N. (2015). Characterization of rudist-dominated units as potential reservoirs in the middle Cretaceous Sarvak Formation, SW Iran. *Facies, 61*, 1–25.

Esteve, C., Lu, Y., Gosselin, J. M., Kramer, R., Aiman, Y., & Bokelmann, G. (2025). Simulation of mineral grades with hard and soft conditioning data: Application to a porphyry copper deposit. *Computational Geosciences, 13*(1), 79–89.

Feng, R., Balling, N., & Grana, D. (2020). Lithofacies classification of a geothermal reservoir in Denmark and its facies-dependent porosity estimation from seismic inversion. *Geothermics, 87*, 101854.

Garcia, L. G., Lôndero, V., Fredere, A. C., Cardoso, M., da Silveira, A. S., & de Oliveira, J. M. (2024). Tridimensional porosity modeling through fuzzy logic and geostatistics. *Geoenergy Science and Engineering, 240*, 212998.

Gomes Gonçalves, Í., & Wellmann, F. (2025). Uncertainty propagation in deep Gaussian process networks. *Mathematical Geosciences, 57*, 1115–1133.

González, J. J., Mery, N., Navarro, F., Díaz, G., Comte, D., & Pichott, S. (2025). Enhancing mining exploration through geostatistical analysis of seismic tomographies at different scales: Improving low-resolution data by high-resolution results. *Natural Resources Research, 34*, 1351–1364.

Grélaud, C., Razin, P., Homewood, P. (2010). Channelized systems in an inner carbonate platform setting: differentiation between incisions and tidal channels (Natih Formation, Late Cretaceous, Oman). In: van Buchem FSP, Gerdes KD, Esteban M (eds) *Mesozoicand Cenozoic carbonate systems of the Mediterranean and the Middle East: stratigraphic and diagenetic reference models*. Geological Society, London, Special Publications 329:163–186.

Haq, B. U. (2014). Cretaceous eustasy revisited. *Global and Planetary Change, 113*, 44–58.

Journel, A. G., & Huijbregts, C. J. (1978). *Mining geostatistics*. Academic Press.

Kamaruzaman, E. H., La Croix, A. D., & Kamp, P. J. (2023). Quantitative seismic geomorphology of sediment conduits on an evolving Miocene slope in Taranaki Basin (New Zealand): The influence of increasing slope gradient through time. *Marine and Petroleum Geology, 152*, 106233.

Kamaruzaman, E. H., La Croix, A. D., & Kamp, P. J. (2024). Interpreting environments of deposition from facies analysis of outcrop versus seismic reflection data: A cautionary tale from the Mount Messenger Formation, Taranaki Basin (New Zealand). *Marine and Petroleum Geology, 167*, 106934.

Kelishami, S. B. A., Rezaei, M., & Mohebian, R. (2022). A new approach to estimate and delineate the geothermal gradient of Iran. *Geothermics, 103*, 102428.

Khayer, K., Roshandel Kahoo, A., Soleimani Monfared, M., Tokhmechi, B., & Kavousi, K. (2022). Target-oriented fusion of attributes in data level for salt dome geobody delineation in seismic data. *Natural Resources Research, 31*, 2461–2481.

Kingma, D.P., & Ba, J. (2014). Adam: A Method for Stochastic Optimization. 3rd International Conference for Learning Representations, San Diego.

Leisi, A., Aftab, S., & Shad Manaman, N. (2024). Poro-acoustic impedance (PAI) as a new and robust seismic inversion attribute for porosity prediction and reservoir characterization. *Journal of Applied Geophysics, 223*, 105351.

Li, W., Yue, D., Wu, S., Shu, Q., Wang, W., Long, T., & Zhang, B. (2020). Thickness prediction for high-resolution stratigraphic interpretation by fusing seismic attributes of target and neighboring zones with an SVR algorithm. *Marine and Petroleum Geology, 113*, 104153.

Li, X., Ao, Y., Guo, S., & Zhu, L. (2019). Combining Regression Kriging with machine learning mapping for spatial variable estimation. *IEEE Geoscience and Remote Sensing Letters, 17*, 27–31.

Lin, L., Zhong, Z., Li, C., Gorman, A., Wei, H., Kuang, Y., Wen, S., Cai, Z., & Hao, F. (2024). Machine learning for subsurface geological feature identification from seismic data: Methods, datasets, challenges, and opportunities. *Earth-Science Reviews, 257*, 104887.

Liner, C.L., Li, C., Gersztenkorn, A., & Smythe, J. (2004). SPICE: A new general seismic attribute*:* 72nd Annual International Meeting, SEG, Expanded Abstracts, 433–436.

Liu, D., Zhao, Z., Cai, Y., & Sun, F. (2024). Characterizing coal gas reservoirs: A multiparametric evaluation based on geological and geophysical methods. *Gondwana Research, 113*, 91–107.

Liu, Y., Carranza, E. J. M., & Xia, Q. (2022). Developments in quantitative assessment and modeling of mineral resource potential: An overview. *Natural Resources Research, 31*, 1825–1840.

Liu, Z., Yang, M., Cheng, J., Wu, D., & Tan, J. (2020). Stochastic isogeometric analysis for the linear stability assessment of plate structures using a Kriging enhanced neural network. *Thin-Walled Structures, 157*, 107120.

Lu, G., Wang, C., Zhang, X., Lu, X., Tang, R., Zhang, S., & Wang, Z. (2025). High-resolution prediction of thin-layer reservoirs based on seismic sedimentology: A case study of the Penglaizhen Formation, Western Sichuan Basin, China. *Natural Resources Research, 34*, 2579–2598.

Lv, A., Cheng, L., Aghighi, M. A., Masoumi, H., & Roshan, H. (2021). A novel workflow based on physics-informed machine learning to determine the permeability profile of fractured coal seams using downhole geophysical logs. *Marine and Petroleum Geology, 131*, 105171.

Marfurt, K.J., & Alves, T.M. (2015). Pitfalls and limitations in seismic attribute interpretation of tectonic features. *Interpretation, 3*.

Maxwell, K., Rajabi, M., & Esterle, J. (2021). Spatial interpolation of coal properties using geographic quantile regression forest. *International Journal of Coal Geology, 248*, 103869.

Maxwell, K., Rajabi, M., Esterle, J., Tivane, M., & Travassos, D. L. (2024). Spatial modelling and classification of altered coal using random forest-based methods at Moatize Basin, Mozambique. *Journal of African Earth Sciences, 215*, 105279.

McQuarrie, N. (2004). Crustal scale geometry of the Zagros fold–thrust belt, Iran. *Journal of Structural Geology, 26*, 519–535.

Mishra, A., Mortazavi, S. A., Dickinson, J., & Haese, R. R. (2025). Improved representation of sub-wireline scale lithological heterogeneity in geological models. *Marine and Petroleum Geology, 174*, 107322.

Misra, S., Chakravarty, A., Bhoumick, P., & Rai, C. S. (2020). Unsupervised clustering methods for noninvasive characterization of fracture-induced geomechanical alterations. In S. Misra, L. Hao, & H. Jiabo (Eds.), *Machine Learning for Subsurface Characterization* (pp. 45–67). Gulf Professional Publishing.

Mohammad Hossain, T., Hermana, M., & Oluwadamilola Olutoki, J. (2024). Porosity prediction and uncertainty estimation in tight sandstone reservoir using non-deterministic XGBoost. *IEEE Access, 12*, 139358–139367.

Mohammadpour, M., Roshan, H., Arashpour, M., & Masoumi, H. (2023). Effect of spatial variability of downhole geophysical logs on machine learning exercises. *International Journal of Coal Geology, 277*, 104333.

Mohammadpour, M., Roshan, H., Arashpour, M., & Masoumi, H. (2024). Machine learning assisted Kriging to capture spatial variability in petrophysical property modelling. *Marine and Petroleum Geology, 167*, 106967.

Mou, N., Carranza, E. J. M., Wang, G., et al. (2023). A framework for data-driven mineral prospectivity mapping with interpretable machine learning and modulated predictive modeling. *Natural Resources Research, 32*, 2439–2462.

Naseer, M. T. (2024). Seismic attributes and inverse quantitative static density–porosity–constraint reservoir simulations of naturally-fractured hydrocarbon-bearing Lower Cretaceous shallow-marine architectures, onshore Indus, Pakistan. *Natural Resources Research, 33*, 213–238.

Naseer, M. T. (2025). Spectral quantitative gas saturation and porosity-constrained lateral variability dynamical simulations of Cretaceous shale gas-bearing deep-water reservoirs, NNE-Indus Onshore. *Natural Resources Research*. https://doi.org/10.1007/s11053-025-10549-z.

Ntibahanana, M., Jianguo, S., Luemba, M., Tondozi, K., Imani, G., & Mohamed, B. (2024). Ensemble of neural networks utilizing seismic attributes for rock-property inversion with uncertainty estimation. *Earth and Space Science, 11*, 2023EA003101.

Nwaila, G. T., & Carranza, E. J. M. (2025). Uncertainty quantification of microblock-based resource models and sequencing of sampling. *Natural Resources Research, 34*, 1927–1952.

Nwaila, G. T., Rose, D. H., Frimmel, H. E., & Ghorbani, Y. (2025). An integrated geodata science workflow for resource estimation: A case study from the Merensky Reef, Bushveld Complex. *Natural Resources Research, 34*, 1301–1329.

Olutoki, J. O., Elsaadany, M., Siddiqui, N. A., Haque, A. E., Ali, S. H., Rashid, A., & Akinyemi, O. D. (2024). Estimating petrophysical properties using geostatistical inversion and data-driven extreme gradient boosting: A case study of Late Eocene McKee Formation, Taranaki Basin, New Zealand. *Results in Engineering, 24*, 103494.

Pedregosa, F., Varoquaux, G., Gramfort, A., Michel, V., Thirion, B., Grisel, O., Blondel, M., Prettenhofer, P., Weiss, R., Dubourg, V., Vanderplas, J., Passos, A., Cournapeau, D., Brucher, M., Perrot, M., Duchesnay, E., & Louppe, G. (2012). Scikit-learn: Machine learning in Python. *Journal of Machine Learning Research, 12*(12), 2825–2830.

Pyrcz, M. J., & Deutsch, C. V. (2014). *Geostatistical Reservoir Modeling*. Oxford University Press.

Rezaei, M., Bahramali Asadi Kelishami, S., & Sangin, S. (2024). Iran's comprehensive heat flow map generated by the Random Forest method and the Sequential Gaussian Simulation. *Geothermics, 118*, 102915.

Rezaei, M., Emami Niri, M., Asghari, O., Talesh Hosseini, S., & Emery, X. (2023). Seismic data integration workflow in pluri-Gaussian simulation: Application to a heterogeneous carbonate reservoir in southwestern Iran. *Natural Resources Research, 32*, 1147–1175.

Sabouhi, M., Moussavi-Harami, R., Kadkhodaie, A., Rezaee, P., & Jalali, M. (2022). A qualitative-quantitative approach for studying the impact of facies and diagenesis control on the rudist biostrome of the Sarvak formation, Abadan Plain, SW Iran. *Journal of Petroleum Science and Engineering, 212*, 110245.

Sergeev, A., Buevich, A., Baglaeva, E., & Shichkin, A. (2019). Combining spatial autocorrelation with machine learning increases prediction accuracy of soil heavy metals. *CATENA, 174*, 425–435.

Song, J., Ntibahanana, M., Luemba, M. L., Tondozi, K., & Imani, G. (2023). Ensemble deep learning-based porosity inversion from seismic attributes. *IEEE Access, 11*, 8761–8772.

Tran, D., Wang, S., & Dong, J. (2025). Influence of spatial borehole density on estimation of geostatistical properties and construction of heterogeneous hydrogeological models. *Engineering Geology, 350*, 107991.

Van Buchem, F., Gaumet, F., Védrenne, V., & Vincent, B. (2006). *Middle East Cretaceous sequence stratigraphy study*. NIOC-IFP.

Verma, N., Kant, R., Maurya, S. P., Kumar, B., Singh, A. P., Hema, G., Singh, R., Singh, K. H., & Sarkar, P. K. (2025). Seismic inversion based on principal component analysis and probabilistic neural network for prediction of porosity from post-stack seismic data. *Earth Science Informatics, 18*, 98.

Vincent, B., van Buchem, F., Bulot, L., Jalali, M., Swennen, R., Hosseini, A., & Baghbani, D. (2015). Depositional sequences, diagenesis and structural control of the Albian to Turonian carbonate platform systems in coastal Fars (SW Iran). *Marine and Petroleum Geology, 63*, 46–67.

Wang, J., Guan, Z., La Croix, A. D., Wang, Q., Ji, L., & Sun, J. (2020). Seismic geomorphology of shallow-water lacustrine deltas in the Paleocene Huanghua Depression, Bohai Bay Basin, eastern China. *Marine and Petroleum Geology, 120*, 104561.

Wang, J., Pang, X., Wang, H., Zhang, Z., Liu, B., & La Croix, A. D. (2024). Seismic geomorphological analysis of submarine fan architecture in the Baiyun Sag, Pearl River Mouth Nasin: Impact of second-order relative sea-level change. *Marine Geology, 469*, 107234.

Yue, D., Li, W., Wang, W. W., Hu, G., Qiao, H., Hu, J., Zhang, M., & Wang, W. W. (2019). Fused spectral-decomposition seismic attributes and forward seismic modelling to predict sand bodies in meandering fluvial reservoirs. *Marine and Petroleum Geology, 99*, 27–44.

Zhang, J., Liu, Y., & Cao, J. (2024). Applying transfer learning to address data scarcity: A case study on LWD gamma ray depth-lag remediation from Volve to another gasfield. *Geoenergy Science and Engineering, 242*, 213231.

Zhang, Z., Wang, G., Carranza, E. J. M., Li, Y., Liu, X., Peng, W., Fan, J., & Xu, F. (2025). Mapping of gold prospectivity in the Qingchengzi Pb–Zn–Ag–Au Polymetallic District, China, with ensemble learning algorithms. *Natural Resources Research, 34*, 41–60.

Zou, C., Zhao, L., Xu, M., Chen, Y., & Geng, J. (2021). Porosity Prediction With Uncertainty Quantification From Multiple Seismic Attributes Using Random Forest. *Journal of Geophysical Research: Solid Earth, 126*.